

Chapter 5

Continuum Models of Ultrashort Laser–Matter Interaction in Application to Wide-Bandgap Dielectrics

Nadezhda M. Bulgakova and Vladimir P. Zhukov

Abstract This chapter is aimed to provide a basic introduction into the principles of modeling approaches which have been developed for getting insight into various interconnected processes initiated inside transparent materials under the action of ultrashort laser pulses with consequences in volumetric modification of material structure. In view of extreme complexity of the problem, modification mechanisms and their driving processes are still far from complete understanding and require further considerable research efforts. Here we focus our consideration on established approaches that treat matter as a continuum medium. They include models describing laser beam propagation through a non-linear transparent glass or crystal with kinetics of electron plasma generation upon beam focusing and attempts to consider further material evolution with insights into thermodynamic state, stress dynamics, and plastic deformations. We underline that the quality of the final structures is determined by the synergetic action of laser excitation/relaxation kinetics, thermodynamics, and mechanics. The chapter does not pretend to completeness and aims to outline main ideas, achievements, and most intriguing findings which are still waiting for explanations and theoretical treatments.

An erratum to this chapter is available at [10.1007/978-3-319-02898-9_16](https://doi.org/10.1007/978-3-319-02898-9_16)

N. M. Bulgakova (✉)
Optoelectronics Research Centre, University of Southampton,
Southampton SO17 1BJ, UK
e-mail: nbul@itp.nsc.ru

N. M. Bulgakova
Institute of Thermophysics SB RAS, 1 Lavrentyev Avenue,
Novosibirsk, Russia630090,

V. P. Zhukov
Institute of Computational Technologies SB RAS, 6 Lavrentyev Avenue,
Novosibirsk, Russia630090,

V. P. Zhukov
Novosibirsk State Technical University, 20 Karl Marx Avenue,
Novosibirsk, Russia630073,

5.1 Introduction

Since 1996 when it was demonstrated that tightly focused femtosecond laser pulses could induce a local internal increase of the refractive index inside bulk transparent glasses [1], the interaction of ultrashort laser pulses with transparent optical materials has attracted a lot of attention as a powerful tool for modification of material properties [2] resulting in generation of surface [3–7] and volume [5, 8–13] periodic structures, densification and refractive index changes [1, 14–20], formation of micro- and nanovoids [9, 21–27], phase transitions (crystallization in amorphous materials and amorphization of crystalline ones) [23, 28]. This gives rise to numerous technological applications based on three-dimensional photonic structures in bulk optical materials, such as waveguides [1, 14–20], Bragg gratings [29, 30], Fresnel zone plates [31], waveplates based on volume nanogratings (VNG) [32], splitters [33], couplers [34, 35], amplifiers [36], rewritable optical memories [37, 38], and computer-generated holograms [39]. As seen from the above citations, the field of laser writing of optical structures in glasses has been rapidly developing during last 15 years and the laser-written structures become the key elements of integrated photonic devices.

While tremendous achievements have been demonstrated toward laser-writing techniques and assembling integrated photonic devices, the physical mechanisms underlying glass modifications have not been fully understood. Here we discuss general principles of applying continuum approaches for numerical modeling of the variety of interconnected processes induced in wide-bandgap dielectric materials by ultrashort pulse laser radiation, starting from the excitation stage and extending to microsecond timescales when a final structure is imprinted into the material matrix. Apart from the fact that the theory and modeling of the laser-induced processes can be the cost reducing tools which may allow choosing the optimal conditions and most appropriate materials for particular desired modifications, they provide a detailed physical understanding of the phenomenon and required material properties for technological applications. We underline, that in view of extreme complexity of the problem, modification mechanisms and their driving processes are still far from complete understanding and require further considerable research efforts as well as developing novel advanced models of both continuum and atomistic/molecular kinds. It should be noticed that this chapter can be considered as a continuation of [40] where the general principles of continuum modeling in application to ultrashort pulsed laser ablation of solids are discussed.

5.2 Ultrafast Laser Excitation of Wide-Bandgap Dielectrics

First we consider the fundamental aspects of ultrafast laser excitation specific for inorganic dielectric materials with an assessment of the state-of-art and further research directions. Successful development of applications based on laser-induced

micro- and nanomodifications of transparent materials requires deep understanding of the whole chain of the intricate processes initiated in dielectrics by fs laser pulses and extending up to millisecond time scales with formation of permanent mechanically deformed and/or chemically modified states. The mentioned chain of the processes starts from material photoionization with creation of seed free electrons. The latter absorb laser energy and, at proper conditions, can produce secondary electrons in collisions with neutral atoms of dielectric matrix, thus generating electron avalanche. This results in considerable change of optical response of the laser-irradiated region towards its “metallization”. Laser beams focused inside the bulk of a transparent material can experience self-focusing starting from a material-dependent threshold power. However, the beam self-focusing collapse is arrested by scattering from the laser produced plasma. In some dielectrics, active recombination of free electrons starts already at sub-ps time scales while in other dielectrics the free electron gas survives up to hundreds of ps [41]. Rapid recombination of free electrons leads to swift heating of the photoexcited region that occurs at ps timescale when heat conduction effects are negligible. As a result of rapid heat release into the atomic subsystem and corresponding pressure rise, thermoelastic stress waves are generated which, depending on the heating level and heat localization, can either completely dissipate, or lead to significant plastic deformations of the material, or even to mechanical damage in the form of micro- and nanovoids in the energy-release zone [42].

It should be underlined that the stress waves not only induce deformations in a hot laser-excited region but also create a hoop stress in an extended cold zone around it. The thermomechanical effects terminate at ~ 10 ns after the laser pulse action when the three-dimensional pressure waves propagate a distance of several micrometers and substantially dissipate. However, under some experimental conditions the ‘mechanical scenario’ can repeat at microsecond timescale after laser pulse termination when the locally released energy spreads due to heat conduction and reaches the regions of ‘cold’ deformation. Softening of the deformed regions can cause secondary redistribution of matter in the laser-affected zone [20] and even emission of secondary thermoelastic waves.

The main mechanisms involved in generation of free carriers in wide-bandgap dielectrics irradiated by visible and near-IR fs laser pulses are the multiphoton and avalanche ionizations. To describe temporal evolution of the free electron density $n_e(t)$, a simple but intuitive rate equation can be written in the following form [43–47]:

$$\frac{\partial n_e(t)}{\partial t} = \sigma_k I^k(t) + \delta I(t) n_e(t). \quad (5.1)$$

Here $I(t)$ is laser intensity; σ_k and δ are the multiphoton ionization (MPI) cross section and the avalanche coefficient respectively; k is the number of photons required for an MPI event. This equation represents a simplest way for estimating the experimental conditions taking into account generating non-homogeneous profiles of the electron density in the surface layer or inside the bulk depth and

changing the optical response of laser-excited matter [43–52]. The excitation process can conventionally be divided into two stages. At the initial stage, free electrons are generated via the multiphoton ionization while avalanche (collisional) ionization develops when a definite “seed” level of the free-electron density is reached which is sufficient to efficiently absorb laser light.

At relatively high radiation intensities, the tunneling ionization mechanism can dominate over multiphoton ionization as determined by the Keldysh parameter $\gamma = \omega(2m_{\text{eff}}E_g)^{0.5}/(eE_L)$ [53–56] where m_{eff} is the effective electron mass; E_L is the electric field of the laser wave; E_g is the band gap width in dielectric materials or ionization potential of individual atoms or molecules; here and everywhere below the symbol e denotes the elementary (positive) charge. The Keldysh parameter can be presented as a ratio between the characteristic time that an electron takes to overcome the energy barrier (the ionization potential whose value can vary in the strong-wave field) and the electromagnetic wave field period. At $\gamma \gg 1$, the MPI mechanism prevails while at $\gamma \ll 1$ the tunneling mechanism becomes dominating. It is widely accepted that, for the tunneling ionization to produce a noticeable effect, the condition $\gamma < 0.5$ should be met. However, a number of experimental facts indicate that multiphoton ionization can dominate even at $\gamma \ll 1$ [55]. These facts gave rise to numerous generalizations of the Keldysh theory of photo-ionization of dielectric materials [56], as well as for atoms and molecules in the gas phase [55].

It must be admitted that the tunneling mechanism of ionization can play a significant role upon focusing on the surface layer of material in vacuum or a low-pressure gas environment. At focusing into material bulk or on its surface in the presence of a dense ambient gas or a liquid surrounding, ionization of medium starts before focus at reaching a definite level of laser intensity. As a result, a high-energy beam is attenuated in its way to the laser focus that leads to the intensity constraints at levels at which the MPI mechanism prevails unambiguously (so-called clamping effect, see [57–59] and Sect. 5.3). It should be noted that, for relatively long wavelengths of femtosecond laser pulses, toward the mid-IR range, the MPI rate strongly decreases and tunneling ionization will inevitably play the dominant role. Although the femtosecond lasers at mid-IR wavelengths are seldom used today, this trend should be mentioned for providing more complete understanding.

The role of avalanche ionization in the breakdown of dielectrics in ultrafast irradiation regimes is still debated [60–63]. Some authors completely deny its existence for sub-ps pulsed irradiation regimes [61] while the others assert that its effects can be even more pronounced with decreasing pulse duration due to a decrease of the potential barrier in a strong laser field (cold avalanche) [63]. Electron recombination in inorganic dielectrics proceeds in the form of trapping in localized states (the recombination rate may be expressed as $R_e = n_e/\tau_{\text{tr}}$ where τ_{tr} is a characteristic recombination time), accompanied by creation of excitons, color centers, non-bridging oxygen hole centers, and other defects [64–67]. Defect generation leads to pronounced incubation effects manifested as a decrease of the

damage threshold in multipulse irradiation regimes [66]. For some materials with very short trapping time (e.g., for fused silica where $\tau_{tr} \approx 150$ fs [67]), the incubation effect, i.e. accumulation of the defect states and their preferential ionization, can appear already during fs laser pulse action.

Based on the above consideration, the kinetic scenario of excitation of an inorganic dielectric material can be described as following. Multiphoton ionization, whose order is determined by the ratio between the bandgap width and photon energy $\hbar\omega$, results in excitation of electrons from the valance band to a low-energy state within the conduction band. At high laser intensities when $\gamma \leq 1$, the tunneling mechanism of ionization becomes dominating in photo-production of free carries. The free electrons may now efficiently absorb laser radiation due to inverse bremsstrahlung. When an electron has absorbed a sufficient amount of the laser energy ($>E_g$), it can collisionally ionize a neutral atom of the material matrix. The development of avalanche (collisional multiplication of free electrons) changes optical properties of the laser-excited region of the material. Spatiotemporal dynamics of optical parameters can be described within the Drude formalism via the complex dielectric function $\varepsilon^*(n_e)$ whose value can be seen as contributions from unexcited matter and generated dense plasma [47, 68]:

$$\varepsilon^*(n_e) \cong 1 + (\varepsilon_g - 1) \left(1 - \frac{n_e}{n_{val}}\right) - \frac{n_e}{n_{cr}} \left(1 + i \frac{1}{\omega\tau_c}\right)^{-1}. \quad (5.2)$$

Here $n_{cr} = \varepsilon_0 n_0 m_{eff} \omega^2 / e^2$ is the critical electron density n_{val} is the total valence-band electron density in the unexcited state; n_0 is the refractive index; ε_g is the dielectric function of unexcited material; ε_0 is the vacuum permittivity; $\omega\tau_c$ is the damping factor [64] determined by the finite electron collision time τ_c (see comments in Sect. 5.3.2). We underline that the reflection coefficient from an inhomogeneous dense plasma at the sample surface layer should be calculated within a multilayer reflection model [42, 68, 69].

Several examples of successful models constructed to simulate laser-induced excitation of surfaces of dielectric and semiconducting materials and their heating dynamics can be found in [41–47, 49–52, 70–72]. They are usually based on the rate equations for charge-carrier generation and recombination and an analog of the two-temperature model either for the average charge-carrier energy or the temperature as a measure of the average energy under the conditions of incomplete thermalization within the electron subsystem. In this section, the main processes in wide-bandgap dielectrics have been outlined for the case of laser beam focusing on the sample surface. Actually the dynamics of laser-induced excitations of dielectric materials is much richer that motivates their utterly wide applications in various optical technologies. In the following sections we concentrate on the peculiarities of optical material modifications by ultrashort laser pulses upon focusing in the bulk depth.

5.3 Volume Modifications of Wide-Bandgap Dielectrics

The regimes of focusing of ultrashort laser pulses inside transparent crystals and glasses which result in local volume modifications of the properties of the irradiated sample are of paramount interests for applications in photonics and optoelectronics among which the main well-established application field is direct writing of waveguide structures, based on a controlled change in the refractive index in laser-modified zones [14–20, 34, 73–80]. Formation of a phase object embedded in the dielectric matrix is caused by rearrangement of bonds in the sample with the displacement of atoms and corresponding change in density, accumulation of stresses, and appearance of defect states. Improved control over modifications in laser-irradiated materials requires detailed studies of both individual laser-induced processes and their interrelations on the timescales from photo-excitation to imprinting a final 3D structure into the matrix of the original material. In the last years, a progress has been achieved in theoretical modeling of laser-excited processes, both during the laser pulse propagation through a transparent material sample and post-irradiation effects though understanding of mechanisms and dynamics of modifications are far from being complete and require further considerable efforts. Here we review the main approaches for investigations of in-volume laser-induced processes and outline future modeling directions.

5.3.1 Propagation of Focused Laser Beams Through Non-linear Absorbing Media

Several types of modeling approaches can be listed which have been developed for studies of propagation of an electromagnetic wave in transparent materials with accounting laser energy absorption. A simple quasi-analytical model [58] can be useful for an estimative analysis of the geometry of laser energy absorption regions and light transmission through the sample. The model relates $\partial I(z,r,t)/\partial t$ and $\partial n_e(z,r,t)/\partial t$ to I and n_e (r and z are the radius and propagation distance of the laser beam). For the regimes considered in [58], it was unambiguously shown that, in transparent solids, the laser intensity is strongly clamped to the maximal reached levels of order of 5×10^{13} W/cm² due to non-linear absorption. Another important observation is that the absorbed laser energy is proportional to the pulse duration. It must be underlined that a more rigorous approach based on solving the non-linear Schrödinger equation supports the latter conclusion, indicating however that at longer pulses the laser energy is deposited into a more localized region [20].

The models of laser light propagation in transparent media based on the non-linear Schrödinger equation (NLSE) are widely utilized for studying the processes of laser excitation of dielectrics in the regimes of modification. The NLSE is an asymptotic parabolic approximation of Maxwell's equations [81] applicable for

describing unidirectional propagation of slowly varying envelopes of laser pulses. This equation describes the self-focusing effect which manifests itself as a laser beam collapse at beam energies beyond a critical value particular for a Kerr medium with the positive non-linear refractive index n_2 . We note that for transparent crystals and glasses the n_2 values are typically in the range of 10^{-16} – 10^{-14} cm^2/W . To account for additional physical effects such as a small non-paraxiality, plasma defocusing, multiphoton ionization, etc., the additional terms are introduced to the scalar models based on the NLSE [18, 19, 82–84]. An important detailed review of NLSE application for various laser beam propagation conditions is given in [85].

A generalized NLSE which takes into account radiation losses for generation of electron plasma on the beam way and plasma-induced changing of the permittivity of the medium can be written in the cylindrically symmetric form as [18, 19, 82–85]:

$$\begin{aligned} \frac{\partial \bar{C}}{\partial z} = & \frac{i}{2k_0} T^{-1} \left(\frac{\partial^2}{\partial r^2} + \frac{1}{r} \frac{\partial}{\partial r} \right) \bar{C} - \frac{ik''}{2} \frac{\partial^2 \bar{C}}{\partial t^2} \\ & + \frac{ik_0 n_2 T}{n_0} \left[(1 - f_R) |\bar{C}|^2 + f_R \int_{-\infty}^t R(t - \tau) |\bar{C}|^2 d\tau \right] \bar{C} \\ & - \frac{\sigma}{2} (1 + i\omega\tau_c) T^{-1} (n_e \bar{C}) - \frac{1}{2} \frac{W_{\text{PI}}(|\bar{C}|) E_g}{|\bar{C}|^2} \bar{C} \end{aligned} \quad (5.3)$$

where \bar{C} is the complex envelope of the electric field strength of the light wave which is assumed to be slowly varying in time. For a Gaussian beam with cylindrical symmetry one has

$$\bar{C}(r, t, 0) = \bar{C}_0 \exp(-r^2/w^2 - t^2/\tau_L^2 - ik_0 r^2/2f). \quad (5.4)$$

Here $\bar{C}_0^2 = 2E_L/(\pi w^2 \tau_L \sqrt{\pi/2})$ is the input pulse intensity; E_L is the pulse energy; $w = w_b(1 + d^2/z_f^2)^{1/2}$ and w_b are the beam radius at the distance d from the geometric focus and the beam waist respectively; the curvature radius f and the focusing distance d are related as $f = (d + z_f^2/d)$; z_f is the Rayleigh length; τ_L is the pulse duration (half-width determined by a decrease in the field envelope by $1/e$ times compared to the maximum value); $k_0 = n_0\omega/c$ and ω are the wave number and the frequency of the carrier wave; n_0 is the refractive index of the medium; c is speed of light; the parameter k'' describes the second-order group velocity dispersion; $E_g = E_{g0} + e^2 \bar{C}^2 / (2cn_0 \epsilon_0 m_r \omega^2)$ is the effective ionization potential in the electromagnetic wave field expressed here via the electric field envelope [19]; m_r is the reduced mass of the electron and hole. Equation (5.3) takes into account the beam diffraction in the transverse direction, group velocity dispersion, the optical Kerr effect with a term corresponding to the delayed (Raman) response of the non-linear material (characterized by the parameter f_R), plasma defocusing, energy absorption due to photoionization and inverse bremsstrahlung. The operator $T = 1 + (i/\omega) \times (\partial/\partial t)$ describes the self-steepening effects. The inverse

bremsstrahlung process is described in the frames of the Drude model with the absorption cross section $\sigma = k_0 e^2 \omega \tau_c / [n_0^2 \omega^2 \epsilon_0 m_e (1 + \omega^2 \tau_c^2)]$. The characteristic collisional time of electrons τ_c is a variable value dependent on electron energy and density (see comments in Sect. 5.3.2).

It should be noted that the linear term in (5.3) gives only an approximate estimation of the absorption efficiency when the free electron concentration considerably increases as the influence of the electron concentration on the absorption cross section is not taken into account. Additionally, the possibility of multiphoton absorption by free electrons is neglected which can be important at relatively high radiation intensities [86]. However, at laser beam focusing into the sample volume, the clamping effect limits the attainable intensities [57–59]. The rate equation describing generation and recombination kinetics of free electrons can be written as:

$$\frac{\partial n_e}{\partial t} = \left[W_{\text{PI}}(|-C|) + \frac{\sigma n_e}{(1 + m_r/m_e) E_g} |-C|^2 \right] \frac{n_{\text{at}} - n_e}{n_{\text{at}}} - \frac{n_e}{\tau_{\text{tr}}}. \quad (5.5)$$

Here n_{at} is the atomic density in the undisturbed material matrix. Equation (5.5) takes into account free electron production in the processes of photoionization and avalanche as well as electron recombination in a trapping-like process associated with local deformations of the atomic lattice (see Sect. 5.2). The rate of photoionization W_{PI} can be described by the Keldysh formalism [53, 54] or in a simplified form for purely multiphoton ionization regimes when the clamping effect limits laser intensity levels to $\gamma \gtrsim 1$ [58].

Numerical investigations based on the NLSE allow elucidating important features of laser pulse propagation through transparent solids such as filamentation [83, 85], clamping [42, 83, 85], strong dependence of the laser energy deposition geometry on pulse duration [19, 42] for different irradiation conditions. Remarkable is the temporal dynamics of laser energy deposition into bulk dielectrics in the modification regimes [19, 42]. On an example of fused silica, it has been demonstrated that only a small fraction of the pulse leading edge, containing 10–15 % of the pulse energy, is absorbed with a high efficiency near and in front of the geometric focus. Due to strong defocusing scattering of the electron plasma generated by the pulse leading edge, the rest laser beam does not fall into the region near the geometric focus. However, as a result of the self-focusing effect, the later parts of the beam are absorbed before the geometric focus and, integrally, they generate the second region of efficient absorption (compare Figs. 11 and 12 in [42]). An important consequence of the complex correlation between self-focusing and plasma defocusing effects is that the local intensity over the whole pulse does not exceed app. 5×10^{13} W/cm², pointing once more to unavoidable intensity clamping. In the context of the clamping effect, the problem of the efficient delivery of laser energy into a local region inside transparent samples remains open. In particular, at high numerical apertures ($\text{NA} \gtrsim 1$) the laser light may be concentrated to a small focal volume with consequences of strong material damage [23].

The validity of the NLSE for ultrashort laser beams focused inside transparent crystals and glasses can be broken down in many situations that is conditioned by

neglecting some small terms upon its derivation from Maxwell’s equations. The condition of a slowly varying envelope limits applications of the NLSE to relatively long laser pulses. For pulse durations of order of 10 fs and shorter, either the NLSE has to be generalized with additional terms to accounting features of such extremely short pulses or, more appropriate, the complete set of Maxwell’s equations are to be used for describing light propagation through a non-linear medium. Another strong limitation imposed on using the NLSE is the requirement of unidirectionality of the light beam. This requirement makes impossible to apply the NLSE to describing tightly focused beams as well as to the cases when dense electron plasma is generated causing light scattering to large angles. Maxwell’s equations are free of the above limitations.

To describe laser beam propagation through an absorbing ionizable medium, Maxwell’s equations are appropriately supplemented to account for multiphoton ionization, multiphoton absorption (that is the depletion of the laser beam due to multiphoton ionization), the Kerr effect, and plasma dispersion while the optical response of the plasma is described in the frames of a plasma fluid model [87]. Maxwell’s equations and the plasma fluid equations are coupled via the free electron current. However, comparing the codes with the NLSE and Maxwell’s equations in application to the same irradiation conditions [88], it has been shown that the NLSE considerably overestimates the generated electron plasma density and, as a result, the locally absorbed laser energy that may lead to misinterpretation of the simulation results. The mentioned overestimation is caused by the fact that the NLSE does not take into account laser light scattering to large angles which becomes significant at relatively high electron densities.

The complete set of Maxwell’s and electron plasma dynamics equations can be solved using a Finite-Difference Time-Domain (FDTD) algorithm. At present, such models represent the best choice for modeling tightly-focused laser beams which can potentially generate dense electron plasma inside transparent dielectric materials. In the three-dimensional (3D) geometry, the model allows to elucidate the effects of laser light polarization [87]. However, such 3D modeling is extremely time and labor consuming and requires unreasonable computer memory resources. In the next section we present a detailed description of a new 2D model based on Maxwell’s equations which however accounts for laser light polarization, including the electron oscillatory motion [88, 89]. Compared to similar 3D codes, the 2D model is a much more time- and cost-efficient tool which allows elucidating many important features of laser light absorption inside transparent solids accompanied by dense electron plasma formation.

5.3.2 2D Model of Electron Plasma Generation upon Laser Beam Focusing Inside Transparent Solids

The basics of the model are essentially similar to those reported in [87] with further development by taking into account avalanche ionization and light dispersion. The model is two-dimensional (2D) that implies cylindrical symmetry of

laser intensity distribution with, however, electron oscillations along laser polarization direction. Maxwell's equations for laser beam propagation through a non-linear absorbing medium can be written in the following form [87–89]:

$$\frac{1}{c} \frac{\partial \vec{D}}{\partial t} - i \frac{\omega}{c} \vec{D} = -\frac{4\pi}{c} \vec{j} + \text{rot} \vec{H} - \frac{8\pi}{c} W_{\text{PI}} E_g \frac{\vec{E}}{|E^2|}, \quad (5.6)$$

$$\frac{1}{c} \frac{\partial \vec{H}}{\partial t} - i \frac{\omega}{c} \vec{H} = -\text{rot} \vec{E}. \quad (5.7)$$

Here we use the standard denotations with E , D , H , and j to be the electric field, the electric displacement field, the magnetic field, and the electric current respectively; all other parameters as in Sect. 5.3.1. In (5.6, 5.7) we assume that the electric field of the beam wave can be presented in the form $\vec{E} = (\vec{E}_0 e^{-i\omega t} + \vec{E}_0^* e^{i\omega t})/2$ and for the plane wave the laser field intensity is expressed as

$$I = \frac{cn_0}{8\pi} |\vec{E}_0|^2.$$

Taking into account the energy clamping effect which saturates the laser intensity at levels with the Keldysh parameter $\gamma > 1$, the multiphoton mechanism of ionization is accepted with the rate $W_{\text{PI}} = \sigma_k I^k (n_{\text{at}} - n_e)/n_{\text{at}}$ reduced by the available ionization centers. Note that we limit consideration to single ionization per atom as a higher order ionization implies a lower ionization cross section whose theory has not yet been developed. Below the simulation results are presented for fused silica for which $k = 6$, $\sigma_6 = 2 \times 10^{-47} \text{ cm}^9/(\text{s W}^6)$ [83], and the atomic (not molecular) density of $6.6 \times 10^{22} \text{ cm}^{-3}$ are adopted. For convenience, the term W_{PI} is rewritten to the form $W_{\text{PI}} = W_{\text{PI}0} (|E^2|/E_*^2)^k (n_{\text{at}} - n_e)/n_{\text{at}}$. Here $W_{\text{PI}0} = 3.7 \times 10^{34} \text{ cm}^{-3} \text{ s}^{-1}$ and $E_*^2 = 8\pi I_*/n_0 c$ with $I_* = 3.5 \times 10^{13} \text{ W/cm}^2$ to be the laser intensity at which the Keldysh parameter $\gamma = 1$. The intensity dependent band gap width $E_g = E_{g0}(1 + e^2 |E^2|/(4m_r \omega^2))$ can be rewritten as $E_g = E_{g0}(1 + |E^2|/(4E_*^2))$; $E_{g0} = 9 \text{ eV}$ and $m_r = 0.64m_e$ [83].

The electric displacement field can be presented as

$$\vec{D} = \vec{E} + \sum_m \vec{P}_m + \vec{P}_{\text{nl}}. \quad (5.8)$$

The linear part of the medium polarization is modeled as a set of oscillators

$$\frac{\partial \vec{P}_m}{\partial t} - i\omega \vec{P}_m = \vec{V}_{Pm}, \quad (5.9)$$

$$\frac{\partial \vec{V}_{Pm}}{\partial t} - i\omega \vec{V}_{Pm} = -\omega_m^2 (\vec{P}_m - B_m \vec{E}), \quad (5.10)$$

where \vec{P}_m and \vec{V}_{Pm} are the local material response and its derivative. For fused silica $m = 1, 2, 3$; $\omega_1 = 27.539 \text{ fs}^{-1}$; $\omega_2 = 16.21 \text{ fs}^{-1}$; $\omega_3 = 0.19034 \text{ fs}^{-1}$;

$B_1 = 0.6962$; $B_2 = 0.4079$; and $B_3 = 0.8975$ [83]. In a particular case of $\vec{E} = \text{const}$, the linear refractive index is expressed as

$$n_0^2 = 1 + \sum_m \frac{B_m \omega_m^2}{\omega_m^2 - \omega^2} = 1 + \sum_m \frac{B_m \lambda_m^2}{\lambda^2 - \lambda_m^2}$$

and for fused silica at $\lambda = 800$ nm we have $n_0 = 1.45$.

In the general case, the non-linear polarization part of (5.8) takes into account the optical Kerr effect with a term corresponding to the delayed Raman-Kerr optical response (see [19, 85]). Here in order to decrease the computation costs, we restrict our consideration to relatively small numerical apertures when the contribution of the delayed Raman-Kerr response is small. Hence, in our case

$$\vec{P}_{\text{nl}} = \frac{c}{4\pi} n_0^2 n_2 |\vec{E}^2| \vec{E}. \quad (5.11)$$

The equations for the density and momentum of free electrons are written as

$$\frac{\partial n_e}{\partial t} = W_{\text{PI}} + W_{\text{av}} - \frac{n_e}{\tau_{\text{tr}}}, \quad (5.12)$$

$$\frac{\partial(n_e \vec{v})}{\partial t} - i\omega n_e \vec{v} = -n_e \frac{e}{m_e} \vec{E} - n_e \frac{\vec{v}}{\tau_c}, \quad (5.13)$$

$$\vec{j} = -n_e e \vec{v}. \quad (5.14)$$

For fused silica $\tau_{\text{tr}} = 150$ fs [67, 90] is used in modeling.

A special comment must be made on the electron collision time τ_c . In the general case, this value is electron density and energy dependent and may be treated similar to [62] with, however, a serious caution in respect of the electron temperature issues. In the fs-laser excited band-gap materials, the electron energy distribution may stay far from equilibrium during the whole pulse duration [54] that does not allow a simple Maxwellian approach for deriving analytical expressions for this characteristic time. The electron collision time is one of the core parameters of the Drude model which is used for evaluation of the electron density in pump-probe measurements of transient dynamics of phase shift and transmission signal intensity [61, 91–93]. For fused silica glass, the *averaged* values of τ_c reported in literature scatter in the range from 0.2 to 23.3 fs [18, 48, 61, 67, 83, 94–97] that is definitely determined by the excitation conditions. As a result, attempts to evaluate the levels of electron plasma densities may lead to an error more than an order of magnitude [88]. A more detailed analysis of Drude-based evaluations of laser-induced electron plasma density upon ultrafast laser excitation will be given in [88]. Here we accept the τ_c value to be equal to 1.27 fs, accounting that the damping factor $\omega\tau_c = 3$ [19]. It must be underlined that, according to simulations, the change in the τ_c value affects but insignificantly the maximum electron density and intensity distributions while influencing the balance between multiphoton and collisional ionization mechanisms. This is

apparently due to a self-consistent nature of beam focusing, self-focusing, plasma absorption and defocusing mechanisms.

From the collisional ionization cross section (see Sect. 5.3.1), one may derive the following avalanche ionization rate

$$W_{\text{av}} = \frac{e^2 \tau_c n_e |\vec{E}^2|}{n_0 c \varepsilon_0 m_e E_g (1 + \omega^2 \tau_c^2) (1 + m_r/m_e)} \frac{n_{\text{at}} - n_e}{n_{\text{at}}}. \quad (5.15)$$

In (5.15) all the parameters are expressed in SI units. The system of (5.6)–(5.14) was solved for the cylindrically symmetric case for fused silica irradiated by femtosecond laser pulses with linear polarization of light at 800 nm wavelength along the x axis, assuming that \vec{E}^2 weakly depends on the azimuthal angle φ . The components of the electric field depend on φ as $E_r = \hat{E}_r(r, z, t) \cos \varphi$; $E_\varphi = \hat{E}_\varphi(r, z, t) \sin \varphi$; $E_z = \hat{E}_z(r, z, t) \cos \varphi$. The validity of cylindrical symmetry is controlled by ensuring the condition $|\hat{E}_r^2| + |\hat{E}_z^2| - |\hat{E}_\varphi^2| \ll |\hat{E}_r^2| + |\hat{E}_z^2| + |\hat{E}_\varphi^2|$. The incoming laser beam is focused inside the bulk at the distance d from the surface and at the sample surface ($z = 0$) it corresponds to the linear polarized light:

$$\hat{E}_r = E_{\text{in}} \exp(-r^2/w^2 - t^2/\tau_L^2 - ik_0 r^2/(2f)), \quad \hat{E}_\varphi = -\hat{E}_r. \quad (5.16)$$

Accordingly, $E_y = 0$; $E_x = \hat{E}_r$; $E_{\text{in}} = [16E_L/(n_0 c w^2 \tau_L \sqrt{\pi/2})]^{1/2}$; all other parameters are defined in Sect. 5.3.1. Note that the generated free electrons oscillate along the x axis while the problem symmetry implies cylindrically symmetric distribution of laser intensity. At the other boundaries, the zero boundary conditions lead to the reflected waves and the necessity of using a large computational region (r_0, z_0). To avoid this, the conditions of the zero Riemann invariants on the incoming characteristics are applied:

$$\begin{aligned} n_0 E_r - B_\varphi &= 0; & n_0 E_\varphi + B_r &= 0 \text{ at } z = z_0; \\ n_0 E_\varphi - B_z &= 0; & n_0 E_z + B_\varphi &= 0 \text{ at } r = r_0. \end{aligned}$$

It must be noted that in (5.12) and (5.13) the terms of the $\text{div}(\vec{\nabla} n_e)$ and $\partial(n_e v_i v_j)/\partial x_j$ kinds and the term involving the Lorentz force have been disregarded. The contributions of the convective terms for the typical irradiation regimes were analyzed and it was found that the plasma density change due to these terms was of order of 10^{-4} as compared to the results with disregarding such terms. As for the Lorentz force, its contribution to the electron current (5.13) is smaller by the factor of v/c as compared to the electric field force and thus it may be safely neglected. For simulations, an implicit numerical scheme was used in the frames of the FDTD method.

Below the results of simulations are presented which are characteristic for the two modification regimes of fused silica, of a relatively low energy pulse (LEP) when volume nanograting structures are obtained at multipulse irradiation ($E_L = 1 \mu\text{J}$, 150 fs pulse duration [8]) and of a higher energy pulse (HEP) above which one may expect the transition to a strong modification [19] resulted from

material melting that may involve creation of void-like structures by single laser pulses ($E_L = 2.5 \mu\text{J}$, 80 fs). Note that the power of both pulses studied is well above the self-focusing threshold (2.8 MW for fused silica [85]).

A comment should be made on the effect of focusing conditions found in the present simulations. Here we limit simulations to the beam waist of $1 \mu\text{m}$. Attempts of beam waist decreasing lead to violation of cylindrical symmetry caused by electron current and, additionally, to the energy nonconservation in the simulation process. For the regimes with $\text{NA} \gtrsim 0.35$ the problem becomes essentially three-dimensional. The realization of a 3D code for describing laser-induced plasma generation inside transparent solids which requires extremely large computational resources is now under development.

Figures 5.1 and 5.2 present snapshots from the calculations [89] which show respectively how the free electron plasma is developing during the laser pulse propagation through the focal zone and how plasma created by the beam front affects propagation of the rest beam. We compare the instantaneous distribution maps of the free electron density (Fig. 5.1) and the laser intensity (Fig. 5.2) for two pulses whose energy differs by 2.5 times. The more energetic pulse has shorter duration so its peak intensity in vacuum is app. 4.6 times higher as compared to the lower-energy pulse. The geometric focus is marked by the white dashed lines while the location of the laser pulse maximum is indicated by the black dot on the z axis. Several important aspects can be noticed. In the LEP regime (Fig. 5.1a, 410 fs), ionization is evidently induced by the very front of the laser pulse when it is approaching the geometrical focus. In the HEP case (Fig. 5.1b) at the same time moment the ionized region is located well before the geometrical focus. This difference is explained by the fact that in the HEP regime the laser intensity level capable to induce considerable ionization is reached earlier relative to the geometric focus as compared to the LEP case. As a result, the pulse front is depleted of energy earlier in space (see Fig. 5.2) and, thus, cannot induce noticeable ionization by this time moment closer to the focus. One can notice that, at the early stages of the LEP propagation, the electron plasma develops rather in the direction toward the laser whereas in the HEP regime the ionization front moves forward with the laser beam. Interesting is that the maximum levels of the plasma density are essentially the same for the two cases and remain considerably subcritical.

Another important difference which has allowed us to realize the features of VNG formation (see [89] for the details) is that in the LEP case the density distribution of the developed electron plasma (at $t \geq 500$ fs) is almost quasi-uniform within the excited region whereas in the HEP case ionization is more localized and one may recognize the signs for double focusing with arising the second maximum (see Fig. 5.1b). During further evolution, the more energetic pulse penetrates deeper to the focal zone with creation plasma behind the geometric focus [88]. Plasma decays quite slowly and, as the simulations show, in three hundred femtoseconds after reaching its maximum it still stays at a level of one-third of the maximum value.

Interesting is that in the LEP regime the snapshots resemble a known hydrodynamic picture of flow over the blunt body where a plasma “body” generated by the

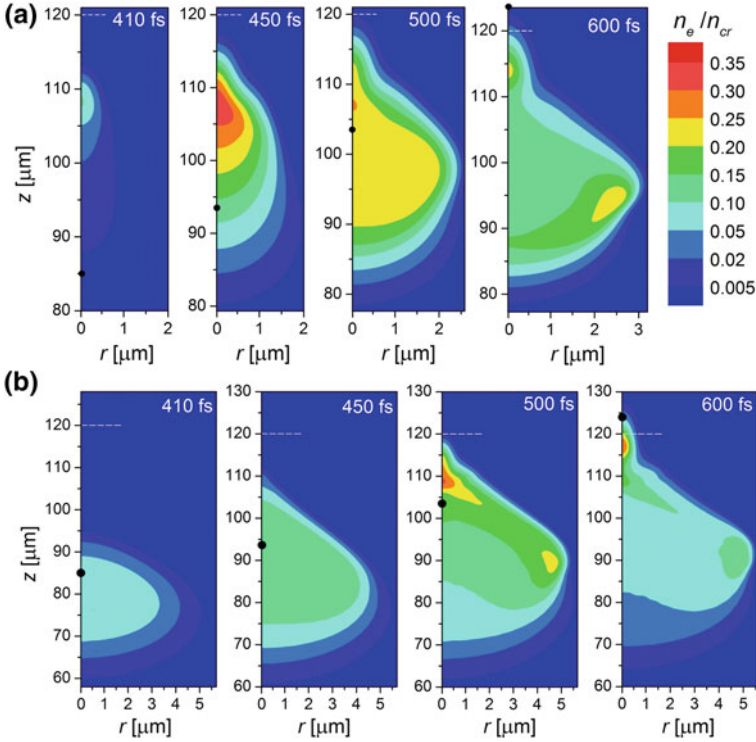


Fig. 5.1 Dynamics of free electron density in fused silica for $E_L = 1 \mu\text{J}$, $\tau_L = 150 \text{ fs}$ (a) and $E_L = 2.5 \mu\text{J}$, $\tau_L = 80 \text{ fs}$ (b) [89]. The laser beam propagates from the *bottom*. The electron density is normalized by the critical electron density, $n_{cr} = \epsilon_0 m_e \omega^2 / e^2$, whose value is $1.74 \times 10^{21} \text{ cm}^{-3}$ for the laser wavelength of 800 nm. Geometric focus of the beam (marked by *dashed lines*) is located at the distance $z = 120 \mu\text{m}$ from the sample surface. At time moment $t = 0$, the maximum of the beam is at $z = 0$ (sample surface) and its location upon beam propagation is marked by the *black dots*. Calculations are started at a negative time moment to ensure that the intensity of the beam front cannot induce any excitation at the initial time moments

beam front completely displaces the rest beam from the plasma region (Fig. 5.2a). The situation is even more dramatic for the HEP regime where strong plasma scattering completely displaces the beam from the beam axis to its periphery from where it again experiences self-focusing behind the plasma region (Fig. 5.2b). Beam self-focusing after strong defocusing (scattering) by the electron plasma is conditioned by the fact that, according to the simulation results, though the laser energy absorbed in the sample during the beam propagation can integrally reach several dozens of percent depending on the beam energy, the beam power still stays well above the self-focusing regime. The simulations clearly demonstrate a strong intensity clamping effect: for the beams with considerably different power the maximum intensity levels differ insignificantly and safely fall to the regimes of *multiphoton ionization*, thus supporting the results of simplified modeling [58].

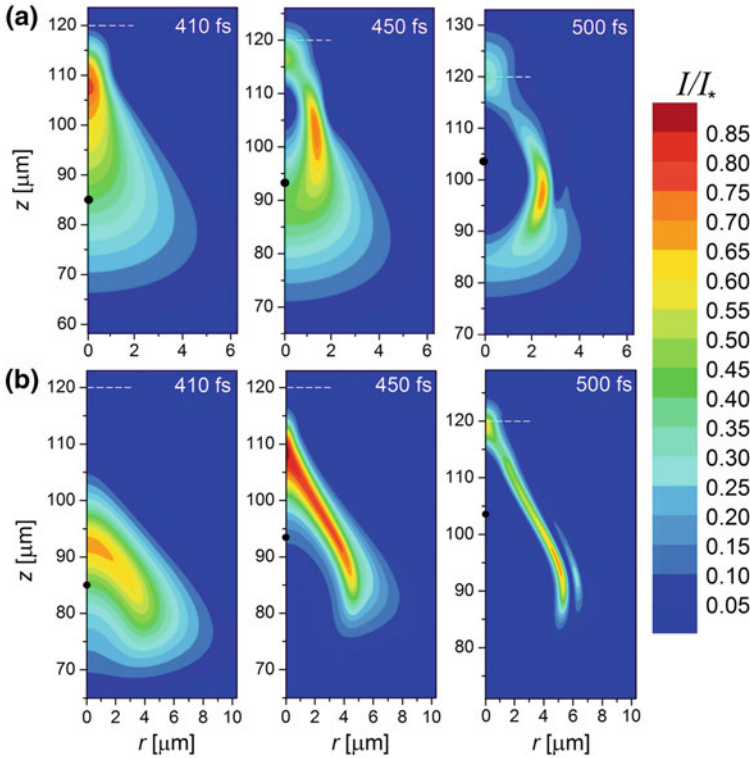


Fig. 5.2 Instantaneous maps of the laser beam intensity for the conditions of Fig. 5.1 [89]. **a** $E_L = 1 \mu\text{J}$, $\tau_L = 150 \text{ fs}$; **b** $E_L = 2.5 \mu\text{J}$, $\tau_L = 80 \text{ fs}$. The intensity is normalized by the value I_* at which the Keldysh parameter $\gamma = 1$ ($I_* = 3.5 \times 10^{13} \text{ W/cm}^2$)

The presented model as well as those reported in [18–20, 23, 41–47, 49–52, 54, 58, 62, 71, 72, 83–87, 94] both simplified and more comprehensive have a great potential for supplementing experimental studies and is a powerful tool to predict and foresee the underlying physics of the observed phenomena. Many detailed aspects which can be overlooked in experiments due to limited resolutions of up-to-date measurement techniques may be revealed with the help of numerical simulations.

5.3.3 Single-Pulse Material Heating and Laser-Induced Stresses

In the model presented above, the absorbed laser energy distribution integrated over the simulation time can be converted to the lattice temperature map, assuming that, at picosecond timescale, all the locally absorbed energy is spend solely to heat the

lattice after electron-lattice thermalization and electron recombination. On the other hand, once the energy absorbed due to electronic excitation is stored in a localized volume of the sample, the level of heating of the material matrix can be evaluated, assuming the definite levels of the density of free electrons and their average energy (temperature). The energy balance may be written in the following form:

$$c_p \rho (T^* - T_0) = n_e e (E_e + E_{g0}). \quad (5.17)$$

Here c_p is the lattice heat capacity, the average energy of free electrons E_e and the band gap energy are expressed in electron-Volt. In (5.17) it is assumed that all the energy from the electronic subsystem including the bandgap energy is finally transmitted to the lattice. Although free electrons are first trapped to the self-trapped exciton (STE) states, the STE population decays at subnanosecond time after excitation [90] and only a small fraction of the STEs (app. 10^{-3}) actually turns to the defect states such as E' -centers [98]. Thus, in (5.17) the energy accumulated in the defect states after single pulse excitation is disregarded. Figure 5.3 [88] shows an example of such E_e - n_e diagram for fused silica which matches pairs of the free electron temperature and density securing material heating to a threshold temperature T^* : annealing (1,400 K), softening (1,858 K [99]), melting (2,006 K [100]), sublimation (2,523 K [100]).

According to a number of studies [42, 45, 54], the typical values of free electron energy in wide-bandgap dielectrics upon excitation with laser pulses of ≥ 100 fs duration are in the range 5–15 eV. This is explainable from the viewpoint of ionization kinetics. Free electrons absorbing photons may produce secondary electrons by collisional ionization if their energy exceeds the material band gap. This sets upper limits on the average electron energy to app. $1.5E_g$ at relatively long pulse durations (at least ≥ 100 fs) when electrons have time to gain enough energy from the beam for developing the avalanche process [62]. The electron number density is much more debated. The pump-probe experiments report the maximum electron densities of $5 \times 10^{19} \text{ cm}^{-3}$ or even lower upon beam focusing into the glass volume (see, e.g., [93]) while the simulation results obtained in the frames of different models give values in the range $\sim (2-8) \times 10^{20} \text{ cm}^{-3}$ [19, 20, 83, 85, 87]. We notice that in the typical modification regimes already single laser pulses produce material expansion (see, e.g., Fig. 5 in [19]). This unambiguously indicates material irreversible expansion in the laser-affected zone which can be produced only if matter is heated at least above the annealing point or even close or above the softening point. Hence, one may roughly circumscribe the electron plasma parameters upon volumetric laser processing of fused silica by the shaded region in Fig. 5.3 where, the higher is the pulse energy, the closer the material state is to the softening point (both higher the electron density and energy). We note that the regimes with plasma parameters above the sublimation point and, partially, above the melting point will result in void (or bubble) generation [88]. Such diagrams can be drawn for any transparent material interesting from the viewpoint of laser processing in order to get a view of the post-irradiation material state.

Fig. 5.3 The diagram matching the energy and density of free electrons excited in fused silica for reaching different levels of heating (annealing, softening, melting, and sublimation points). The *dashed lines* are added for heating silica glass from 300 K to several fixed temperature levels (350, 500, and 800 K)

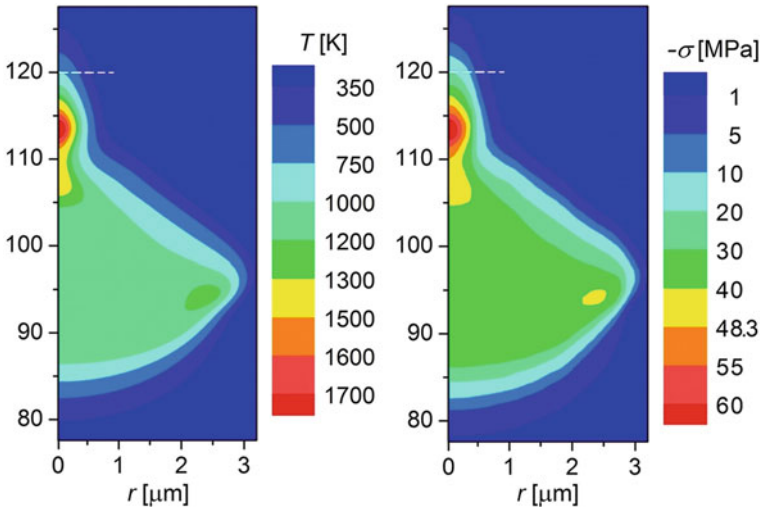
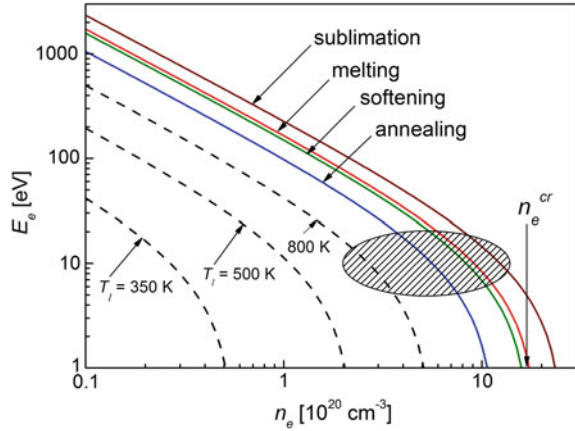


Fig. 5.4 The maps of the temperature (*left*) and thermal stress (*right*) after the laser beam propagation through fused silica sample for the LEP regime that corresponds to Figs. 5.1a and 5.2a. The stress level of 48.3 MPa is the static tensile strength value tabulated for fused silica

Using Expression (5.17), the spatial distributions of the lattice temperature may be mapped while, applying the thermoelastoplastic model [20, 101], we can obtain instantaneous distributions of the material stress. An example is given in Fig. 5.4 for the LEP case which corresponds to Figs. 5.1a and 5.2a. As can be seen, the matter stays below the melting point (Fig. 5.4, left). The compressive stress has a maximum of ~ 65 MPa that is higher than the material tensile strength of 48.3 MPa tabulated for fused silica under the normal conditions (Fig. 5.4, right). The tensile stress which is generated upon material expansion from the compressed state may have the same or lower amplitude as compared to preceded

compressed stress. Although the transient tensile stress may exceed the material static strength, materials can usually withstand the levels of the dynamic stresses much higher than the static ones. However, the induced high stress gradients of order of (60–70) MPa/ μm (Fig. 5.4b) will result in formation of a strong compressive wave which will lead to rarefaction of the regions of the enhanced temperature and creation of a densified envelope surrounding the expanded core [20]. If the matter is heated above the melting point, its strength drops by several orders of magnitude. Hence, it may be expected that at higher laser energies bubble/void formation may be observed (see, e.g., [19, 27]). According to simulations, our HEP regime (see Figs. 5.1b, 5.2b) falls to a boundary above which bubble/void formation may be already expected [88]. We underline that, for bubble/void formation, reaching stresses of order of the Young's modulus is far not obligatory though such stress levels may be attainable by beam focusing with high numerical apertures ($\text{NA} \gtrsim 1$), resulting in creation of warm dense matter conditions [23, 102].

5.3.4 Comments on Multipulse Irradiation Regimes

Laser writing of local structures of modified matter in transparent materials for different application purposes is performed mainly in a gentle manner by multipulse irradiation at relatively low beam energies ($\leq 1 \mu\text{J}$) in order to avoid material failure. Depending on a desired final structure, writing is performed either into a fixed volume inside the sample or by moving the sample relative to the laser beam focus with different scanning speeds. Under such conditions, accumulation of laser-induced modifications from pulse to pulse is a topic of prime importance for designing structures with desired properties.

To provide crack-free laser writing of permanent structures with positive refractive index changes for waveguiding applications, laser irradiation should be applied gently in an accumulative manner avoiding conditions of material failure. Several accumulation mechanisms responsible for gentle modification of transparent materials towards waveguiding properties are established among which heat accumulation is best demonstrated [15, 76, 103–109]. At relatively high repetition rates, the energy absorbed at the focal volume from each pulse has no time to diffuse out completely before the subsequent pulse, thus forming a point source of heat. The process of heat accumulation upon waveguide writing can be controlled by several means: variation of pulse energy, pulse repetition rate, scanning speed, and focusing conditions. A simple analysis of the heat accumulation effect can be performed on the basis of the heat flow equation. The characteristic time of heat propagation by the distance r can be estimated as $t_{\text{heat}} \sim r^2(\rho c/\lambda)$ where ρ , c , and λ are the material density, heat capacity, and thermal conductivity respectively. For fused silica, the heat wave propagates by $\sim 1 \mu\text{m}$ during first microsecond after the laser pulse termination while complete dissipation of heat from the focal volume of few micrometer size may take time up to dozens of microseconds (note

that, according to the heat flow equation, dissipation is determined by both the thermal conductivity and the temperature gradient and is slowing down with decreasing the latter). For unmoved silicate glass samples at a pulse energy sufficient for noticeable heating of a localized focal zone, pulse repetition rate of order of 100 kHz and higher is required for pronounced accumulation of heat [106]. For fixed laser pulse energy, the higher the repetition rate is, the fewer pulses are required for considerable accumulative heating of the sample within the focal volume. The morphologies of laser-induced modifications with and without the heat-accumulation regimes may be completely different [108]. The structures produced at low repetitions rates are strongly localized. In fact, only a zone absorbing laser energy is modified while surrounding material looks essentially unchanged. At high repetition rates when the conditions for heat accumulation are realized, an extended volume around the light absorbing region shows signs of modification where one can recognize two distinct zones, the interior with indications of material melting and a halo whose outer boundary is presumably determined by reaching the softening temperature upon laser exposure (see Fig. 1 in [108]).

Translating the sample relative to the laser pulse imposes further restrictions on the minimal repetition rate. The requirement here is the number of pulses coupling with the same sample volume upon translation which should be sufficient for heat accumulation inducing local modification. Increased laser pulse energy or a higher repetition rate result in larger radius of heat modified zone and allow faster translating for producing a similar final structure that is beneficial for practical applications [75]. This process must be thoroughly controlled as excessive heat accumulation causes material failure with formation of random or organized voids [109]. On the other hand, such regimes are exploited for writing microfluidic channels for biosensing and biomicrochip applications [78, 110, 111]. However, in such regimes heat accumulation cannot be considered separately from the formation of highly stressed states of matter resulting in stress wave emission with possible consequences in the form of plastic deformations. Another parameter considerably influencing the modification structure is focusing. As an example, a laser pulse with the energy of only 20 nJ applied at tight focusing (0.65 NA) induces a similar refractive index change (though in a smaller volume) as the 1- μ J pulse with loose focusing (~ 0.1 NA) [103]. Hence, a tighter focusing, being energetically advantageous as compared to loose focusing conditions, results also in miniaturization of written structures. This has especially strikingly demonstrated with $NA > 1$ [23, 102].

In spite of the evidence that accumulative processes play a key role in glass modification, the accumulative modification mechanisms have not completely been understood. Additionally, it must be remarked that in multipulse irradiation regime each subsequent pulse arrives to already modified matter as compared to the previous pulses. Thus, a gradual accumulation of the defect states with larger excitation cross sections makes excitation easier for subsequent pulses. On the other hand, the refractive index also varies due to defect generation [67], local densification/rarefaction, and stress accumulation, thus affecting laser pulse

propagation through the modified volume. However, such aspects of laser micromachining still require further studies, both experimental and theoretical, while their modeling is still in a very primeval state. More detailed reviews of this and other issues on ultrafast laser writing in transparent materials can be found in [112, 113].

5.4 Concluding Remarks

In this chapter we have reviewed an intricate interconnection of the physical processes which can be initiated by ultrashort laser pulses inside transparent solids with consequences in the form of structural material modifications. Some modification kinds have already been utilized in various applications such as integrated optical devices while the others are still waiting for adoption to practice. In the majority of technologies based on laser directly-written material modifications, practice develops well ahead as compared to fundamental understanding of underlying physics and chemistry of the phenomena. On one hand, this is conditioned by possibilities of using new discovered structures and phenomena for growing practice demands but, on the other hand, the effectiveness of laser-based direct writing is of limited utility namely because of lacking knowledge-based optimization. One of the striking examples is volume nanograting formation inside fused silica glass whose nature is still highly debated. After discovery in 2003 [8], the VNGs, in particular in fused silica, have become an exciting object for research [see, e.g., 9, 10, 114–116] and an important element for a variety of existing and promising applications in optics and photonics [117]. The origin of the VNGs is attributed to several mechanisms such as interference of plasma waves with laser light [8, 9], formation of nanoplasmas followed by self-organization into nanoplanes through the memory effects [10, 38], and interference of the two modes of ultrashort-living excitons-polaritons [118]. All these explanations remain to be unconvincing.

We note that the VNG explanation by light interference with the main mode of plasma oscillations requires the near-critical electron density and the free electron energies of hundreds or even thousands eV [8]. Such electron energies lead to creation of multiply charged ions, complete braking of bonds inside the excited area, followed by hydrodynamics similar to that described in [23, 102]. The exciton-polariton interaction [118] may be important only at low densities of low-energetic free electrons which rapidly transform into self-trapped excitons after excitation to the conduction band [90, 119]. At $n_e \geq 10^{19} \text{ cm}^{-3}$, the exciton-polariton interaction is to be heavily screened by the electron plasma when it begins to efficiently absorb laser energy. The nanoplasma mechanism of nanograting formation may be initiated between the two extremes mentioned above with evolution toward the critical density at nanoplane sites [10, 38] though the evolution routes remain vague. Modeling presented in Sect. 5.3.2 has allowed us to get aware on a paramount role of collective behavior of free electron plasma excited on the surface

and inside transparent solids, the topic which still remains unexplored though well-established in dense plasma physics. As a result, a new mechanism of VNG formation based on scattering of the laser light by developing electron plasma culminating with ionization scattering instability [120] has been proposed [89]. Additionally, writing anisotropy inside isotropic materials with tilted laser pulses observed in [11] has also been explained on the basis of plasma scattering effects within the model described in Sect. 5.3.2 [89]. We stress that the above explanations would not be possible without the comprehensive modeling efforts.

Returning to the importance of the different continuum approaches, we refer readers to [40] and again underline the incipient stage in modeling efforts to investigate the whole route of laser-induced evolution of transparent materials towards obtaining new unusual practicable properties. Finally, we repeat that the theory and modeling of the laser-induced processes can be the cost reducing tools which may allow choosing the optimal conditions and most appropriate materials for particular desired modifications and provide a detailed physical understanding of the phenomenon and required material properties for technological applications.

The authors acknowledge financial support of the European Commission funding under the 7th Framework Programme (Marie Curie International Incoming Fellowship grant of the principal author, No. 272919) and of the Russian Foundation for Basic Research (RFBR project No. 12-01-00510) which made possible to develop the above-described comprehensive modeling tool.

References

1. K.M. Davis, K. Miura, N. Sugimoto, K. Hirao, *Opt. Lett.* **21**, 1729 (1996)
2. R.R. Gattass, E. Mazur, *Nat. Photonics* **2**, 219 (2008)
3. P.A. Temple, M.J. Soileau, *IEEE J. Quantum Electron.* **17**, 2067 (1981)
4. N.C. Kerr, B.A. Omar, S.E. Clark, D.C. Emmony, *J. Phys. D* **23**, 884 (1990)
5. J. Gottmann, D. Wortmann, M. Hörstmann-Jungemann, *Appl. Phys. A* **255**, 5641 (2009)
6. B. Dusser, Z. Sagan, H. Soder, N. Faure, J.P. Colombier, M. Jourlin, E. Audouard, *Opt. Express* **18**, 2913 (2010)
7. S.K. Das, K. Dasari, A. Rosenfeld, R. Grunwald, *Nanotechnology* **21**, 155302 (2010)
8. Y. Shimotsuma, P.G. Kazansky, J.R. Qiu, K. Hirao, *Phys. Rev. Lett.* **91**, 247405 (2003)
9. Y. Shimotsuma, K. Hirao, J.R. Qiu, P.G. Kazansky, *Mod. Phys. Lett. B* **19**, 225 (2005)
10. V.R. Bhardwaj, E. Simova, P.P. Rajeev, C. Hnatovsky, R.S. Taylor, D.M. Rayner, P.B. Corkum, *Phys. Rev. Lett.* **96**, 057404 (2006)
11. P.G. Kazansky, W.J. Yang, E. Bricchi, J. Bovatsek, A. Arai, Y. Shimotsuma, K. Miura, K. Hirao, *Appl. Phys. Lett.* **90**, 151120 (2007)
12. R.S. Taylor, C. Hnatovsky, E. Simova, P.P. Rajeev, D.M. Rayner, P.B. Corkum, *Opt. Lett.* **32**, 2888 (2007)
13. G. Cheng, K. Mishchik, C. Maclair, E. Audouard, R. Stoian, *Opt. Exp.* **17**, 9515 (2009)
14. K. Miura, J. Qiu, H. Inouye, T. Mitsuyu, K. Hirao, *Appl. Phys. Lett.* **71**, 3329 (1997)
15. C.B. Schaffer, A. Brodeur, J.F. García, E. Mazur, *Opt. Lett.* **26**, 93 (2001)
16. Z. Wang, K. Sugioka, Y. Hanada, K. Midorikawa, *Appl. Phys. A* **88**, 699 (2007)
17. W. Yang, C. Corbari, P.G. Kazansky, K. Sakaguchi, I.C.S. Carvalho, *Opt. Exp.* **16**, 16215 (2008)

18. S.W. Winkler, I.M. Burakov, R. Stoian, N.M. Bulgakova, A. Husakou, A. Mermillod-Blondin, A. Rosenfeld, D. Ashkenasi, I.V. Hertel, Appl. Phys. A **84**, 413 (2006)
19. I.M. Burakov, N.M. Bulgakova, R. Stoian, A. Mermillod-Blondin, E. Audouard, A. Rosenfeld, A. Husakou, I.V. Hertel, J. Appl. Phys. **101**, 043506 (2007)
20. A. Mermillod-Blondin, I.M. Burakov, Y.P. Meshcheryakov, N.M. Bulgakova, E. Audouard, A. Rosenfeld, A. Husakou, I.V. Hertel, R. Stoian, Phys. Rev. B **77**, 104205 (2008)
21. E.N. Glezer, E. Mazur, Appl. Phys. Lett. **71**, 882 (1997)
22. W. Watanabe, K. Itoh, Opt. Exp. **10**, 14 (2002)
23. S. Juodkazis, K. Nishimura, S. Tanaka, H. Misawa, E.G. Gamaly, B. Luther-Davies, L. Hallo, P. Nicolai, V.T. Tikhonchuk, Phys. Rev. Lett. **96**, 166101 (2006)
24. R. Graf, A. Fernandez, M. Dubov, H.J. Brueckner, B.N. Chichkov, A. Apolonski, Appl. Phys. A **87**, 21 (2007)
25. H.Y. Sun, J. Song, C.B. Li, J. Xu, X.S. Wang, Y. Cheng, Z.Z. Xu, J.R. Qiu, T.Q. Jia, Appl. Phys. A **88**, 285 (2007)
26. A. Mermillod-Blondin, J. Bonse, A. Rosenfeld, I.V. Hertel, Y.P. Meshcheryakov, N.M. Bulgakova, E. Audouard, R. Stoian, Appl. Phys. Lett. **94**, 041911 (2009)
27. M. Beresna, M. Gecevičius, N.M. Bulgakova, P.G. Kazansky, Opt. Express **19**, 18989 (2011)
28. V. Koubassov, J.F. Laprise, F. Théberge, E. Förster, R. Sauerbrey, B. Müller, U. Glatzel, S.L. Chin, Appl. Phys. A **79**, 499 (2004)
29. L. Sudrie, M. Franco, B. Prade, A. Mysyrowicz, Opt. Commun. **171**, 279 (1999)
30. K. Kintaka, J. Nishii, Y. Kawamoto, A. Sakamoto, P.G. Kazansky, Opt. Lett. **27**, 1394 (2002)
31. E. Bricchi, J.D. Mills, P.G. Kazansky, B.G. Klappauf, Opt. Lett. **27**, 2200 (2002)
32. M. Beresna, P.G. Kazansky, Opt. Lett. **35**, 1662 (2010)
33. J. Liu, Z. Zhang, S. Chang, C. Fluerau, C.P. Grover, Opt. Comm. **253**, 315 (2005)
34. A.M. Streltsov, N.F. Borrelli, Opt. Lett. **26**, 42 (2001)
35. K. Minoshima, A.M. Kowalevich, E.P. Ippen, J.G. Fujimoto, Opt. Exp. **10**, 645 (2002)
36. R. Osellame, S. Taccheo, G. Cerullo, M. Marangoni, D. Polli, R. Ramponi, P. Laporta, S. De Silvestri, Electron. Lett. **38**, 964 (2002)
37. Y. Shimotsuma, M. Sakakura, K. Miura, J. Qiu, P.G. Kazansky, K. Fujita, K. Hirao, J. Nanosci. Nanotechnol. **7**, 94 (2007)
38. R. Taylor, C. Hnatovsky, E. Simova, Laser Photonics Rev. **2**, 26 (2008)
39. W.J. Cai, A.R. Libertun, R. Piestun, Opt. Express **14**, 3785 (2006)
40. N.M. Bulgakova, R. Stoian, A. Rosenfeld, I.V. Hertel, in *Laser-Surface Interactions for New Material Production*, vol. 130, ed. by A. Miotello, P.M. Ossi, Springer Series in Material Science (Springer, Berlin 2009), p. 81
41. I.M. Burakov, N.M. Bulgakova, R. Stoian, A. Rosenfeld, I.V. Hertel, Appl. Phys. A **81**, 1639 (2005)
42. N.M. Bulgakova, R. Stoian, A. Rosenfeld, Quantum Electron. **40**, 966 (2010)
43. A.S. Epifanov, Sov. Phys. JETP **35**, 897 (1975)
44. B.G. Gorshkov, A.S. Epifanov, A.A. Manenkov, Sov. Phys. JETP **49**, 309 (1979)
45. D. Arnold, E. Cartier, Phys. Rev. B **46**, 15102 (1992)
46. B.C. Stuart, M.D. Feit, A.M. Rubenchik, B.W. Shore, M.D. Perry, Phys. Rev. Lett. **74**, 2248 (1995)
47. B.C. Stuart, M.D. Feit, S. Herman, A.M. Rubenchik, B.W. Shore, M.D. Perry, Phys. Rev. B **53**, 1749 (1995)
48. S.S. Mao, F. Quéré, S. Guizard, X. Mao, R.E. Russo, G. Petite, P. Martin, Appl. Phys. A **79**, 1695 (2004)
49. N.M. Bulgakova, R. Stoian, A. Rosenfeld, I.V. Hertel, W. Marine, E.E.B. Campbell, Appl. Phys. A **81**, 345 (2005)
50. A. Vogel, J. Noack, G. Hüttman, G. Paltauf, Appl. Phys. B **81**, 1015 (2005)
51. M. Mero, W. Rudolph, D. Ristau, K. Starke, Phys. Rev. B **71**, 115109 (2005)
52. N.S. Shcheblanov, T.J.Y. Derrien, T.E. Itina, AIP Conf. Proc. **1464**, 79 (2012)

53. L.V. Keldysh, *Sov. Phys. JETP* **20**, 1307 (1965)
54. A. Kaiser, B. Rethfeld, M. Vicanek, G. Simon, *Phys. Rev. B* **61**, 11437 (2000)
55. K. Mishima, M. Hayashi, J. Yi, S.H. Lin, H.L. Selzle, E.W. Schlag; *Phys. Rev. A* **66**, Paper 053408 (2002)
56. V.E. Gruzdev, *Phys. Rev. B* **75**, 205106 (2007)
57. A. Becker, N. Akozbek, K. Vijayalakshmi, E. Oral, C.M. Bowden, S.L. Chin, *Appl. Phys. B* **73**, 287 (2001)
58. D.M. Rayner, A. Naumov, P.B. Corkum, *Opt. Express* **13**, 3208 (2005)
59. Q. Sun, F. Liang, R. Vallee, S.L. Chin, *Opt. Lett.* **33**, 2713 (2008)
60. M. Lenzner, J. Krüger, S. Sartania, Z. Cheng, C. Spielmann, G. Mourou, W. Kautek, F. Krausz, *Phys. Rev. Lett.* **80**, 4076 (1998)
61. F. Quééré, S. Guizard, P. Martin, *Europhys. Lett.* **56**, 138 (2001)
62. G.M. Petrov, J. Davis, *J. Phys. B* **41**, 025601 (2008)
63. P.P. Rajeev, M. Gertsvolf, P.B. Corkum, D.M. Rayner, *Phys. Rev. Lett.* **102**, 083001 (2009)
64. S.C. Jones, P. Braunlich, R.T. Casper, X.-A. Shen, P. Kelly, *Opt. Engin.* **28**, 1039 (1989)
65. K. Tanimura, H. Fujiwara, T. Suzuki, *Nucl. Instrum. Meth. B* **116**, 26 (1996)
66. J. Krüger, M. Lenzner, S. Martin, M. Lenner, C. Spielman, A. Fiedler, W. Kautek, *Appl. Surf. Sci.* **208**, 233 (2003)
67. P. Martin, S. Guizard, Ph. Daguzan, G. Petite, P. D'Oliveira, P. Maynadier, M. Pedrix, *Phys. Rev. B* **55**, 5799 (1997)
68. K. Sokolowski-Tinten, D. von der Linde, *Phys. Rev. B* **61**, 2643 (2000)
69. Sh. Furman, A.V. Tikhonravov, *Basics of Optics of Multilayer Systems* (Editions Frontières, Gif-sur-Yvette, 1992)
70. N.M. Bulgakova, R. Stoian, A. Rosenfeld, I.V. Hertel, E.E.B. Campbell, *Phys. Rev. B* **69**, Paper 054102 (2004)
71. C. Mézel, A. Bourgeade, L. Hallo, *Phys. Plasmas* **17**, 113504 (2010)
72. B. Chimier, O. Utéza, N. Sanner, M. Sentis, T. Itina, P. Lassonde, F. Légaré, F. Vidal, J.C. Kieffer, *Phys. Rev. B* **84**, 094104 (2011)
73. C. Florea, K.A. Winick, *J. Lightwave Tech.* **21**, 246 (2003)
74. W. Watanabe, T. Asano, K. Yamada, K. Itoh, J. Nishii, *Opt. Lett.* **28**, 2491 (2003)
75. L. Shah, A. Arai, S. Eaton, P. Herman, *Opt. Express* **13**, 1999 (2005)
76. S.M. Eaton, H.B. Zhang, P.R. Herman, F. Yoshino, L. Shah, J. Bovatsek, A.Y. Arai, *Opt. Express* **13**, 4708 (2005)
77. K. Suzuki, V. Sharma, J.G. Fujimoto, E.P. Ippen, *Opt. Express* **14**, 2335 (2006)
78. H.Y. Sun, F. He, Z.H. Zhou, Y. Cheng, Z.Z. Xu, K. Sugioka, K. Midorikawa, *Opt. Lett.* **32**, 1536 (2007)
79. C. Mauclair, G. Cheng, N. Huot, E. Audouard, A. Rosenfeld, I.V. Hertel, R. Stoian, *Opt. Express* **17**, 3531 (2009)
80. A. Ferrer, A.R. de la Cruz, D. Puerto, W. Gawelda, J.A. Valles, M.A. Rebolledo, V. Berdejo, J. Siegel, J. Solis, *J. Opt. Soc. Am. B* **27**, 1688 (2010)
81. R. Temam, A. Miranville, *Mathematical Modeling in Continuum Mechanics* (Cambridge University Press, UK, 2005)
82. A.L. Gaeta, *Phys. Rev. Lett.* **84**, 3582 (2000)
83. A. Couairon, L. Sudrie, M. Franco, B. Prade, A. Mysyrowicz, *Phys. Rev. B* **71**, 125435 (2005)
84. V.P. Kandidov, S.A. Shlenov, O.G. Kosareva, *Quantum Electron.* **39**, 205 (2009)
85. A. Couairon, A. Mysyrowicz, *Phys. Rep.* **441**, 47 (2007)
86. H. Bachau, A.N. Belsky, I.B. Bogatyrev, J. Gaudin, G. Geoffroy, S. Guizard, P. Martin, Y.V. Popov, A.N. Vasil'ev, B.N. Yatsenko, *Appl. Phys. A* **98**, 679 (2010)
87. K.I. Popov, C. McElcheran, K. Briggs, S. Mack, L. Ramunno, *Opt. Express* **19**, 271 (2010)
88. N.M. Bulgakova, V.P. Zhukov, S.V. Sonina, Yu.P. Meshcheryakov, to be published
89. N.M. Bulgakova, V.P. Zhukov, Yu.P. Meshcheryakov, *Appl. Phys. B* (2013). doi:[10.1007/s00340-013-5488-0](https://doi.org/10.1007/s00340-013-5488-0)

90. D. Grojo, M. Gertszolf, S. Lei, T. Barillot, D.M. Rayner, P.B. Corkum, *Phys. Rev. B* **81**, 212301 (2010)
91. V.V. Temnov, K. Sokolowski-Tinten, P. Zhou, B. Rethfeld, V.E. Gruzdev, A. El-Khamawy, D. von der Linde, *Proc. SPIE* **5448**, 1119 (2004)
92. V.V. Temnov, K. Sokolowski-Tinten, P. Zhou, A. El-Khamhawy, D. von der Linde, *Phys. Rev. Lett.* **97**, 237403 (2006)
93. D.G. Papazoglow, I. Zergioti, S. Tsortzakis, *Opt. Lett.* **32**, 2055 (2007)
94. A.Q. Wu, I.H. Chowdhury, X. Xu, *Phys. Rev. B* **72**, 085128 (2005)
95. Q. Sun, H. Jiang, Y. Liu, Z. Wu, H. Yang, Q. Gong, *Opt. Lett.* **30**, 320 (2005)
96. A. Mermillod-Blondin, C. Maucclair, J. Bonse, R. Stoian, E. Audouard, A. Rosenfeld, I.V. Hertel, *Rev. Sci. Instrum.* **82**, 033703 (2011)
97. L. Sudrie, A. Couaron, M. Franco, B. Lamouroux, B. Prade, S. Tzortzakis, A. Mysyrowicz, *Phys. Rev. Lett.* **89**, 186601 (2002)
98. G. Petite, S. Guizard, P. Martin, F. Quéré, *Phys. Rev. Lett.* **83**, 5182 (1999)
99. X.R. Zhang, X. Xu, A.M. Rubenchik, *Appl. Phys. A* **79**, 945 (2004)
100. J. Siegel, K. Ettrich, E. Welsch, E. Matthias, *Appl. Phys. A* **64**, 213 (1997)
101. Y.P. Meshcheryakov, N.M. Bulgakova, *Appl. Phys. A* **82**, 363 (2006)
102. E.G. Gamaly, A. Vailionis, V. Mizeikis, W. Yang, A.V. Rode, S. Juodkazis, *High Energy Density Phys.* **8**, 13 (2012)
103. C.B. Schaffer, J.F. García, E. Mazur, *Appl. Phys. A* **76**, 351 (2003)
104. R.R. Gattass, L.R. Cerami, E. Mazur, *Opt. Express* **14**, 5279 (2006)
105. I. Miyamoto, A. Horn, J. Gottmann, *J. Laser Micro/Nanoeng.* **2**, 7 (2007)
106. H. Zhang, A.M. Eaton, J. Li, P.R. Herman, *J. Phys: Conf. Ser.* **59**, 682 (2007)
107. M. Sakakura, M. Shimizu, Y. Shimotsuma, K. Miura, K. Hirao, *Appl. Phys. Lett.* **93**, 231112 (2008)
108. M. Shimizu, M. Sakakura, M. Ohnishi, Y. Shimatsuma, T. Nakaya, K. Miura, K. Hirao, *J. Appl. Phys.* **108**, 073533 (2010)
109. Y. Bellouard, M.-O. Hongler, *Opt. Express* **19**, 6807 (2011)
110. Y. Liao, Y. Ju, L. Zhang, F. He, Q. Zhang, Y. Shen, D. Chen, Y. Cheng, Z. Xu, K. Sugioka, K. Midorikawa, *Opt. Lett.* **35**, 3225–3227 (2010)
111. K. Sugioka, Y. Hanada, K. Midorikawa, *Laser Photon. Rev.* **4**, 386 (2010)
112. N.M. Bulgakova, in *Ultrafast Laser Processing: From Micro- to Nanoscale*, ed. by K. Sugioka, Y. Cheng (Pan Stanford Publishing, 2013), p. 48
113. K. Miura, K. Hirao, Y. Shimotsuma, M. Sakakura, in *Ultrafast Laser Processing: From Micro- to Nanoscale*, ed. by K. Sugioka, Y. Cheng (Pan Stanford Publishing, 2013), p. 251
114. M. Hörstmann-Jungemann, J. Gottmann, M. Keggenhoff, *J. Laser Micro/Nanoeng.* **4**, 135 (2009)
115. K. Mishchik, G. Cheng, G. Huo, I.M. Burakov, C. Maucclair, A. Mermillod-Blondin, A. Rosenfeld, Y. Ouerdane, A. Boukenter, O. Parriaux, R. Stoian, *Opt. Express* **18**, 24809 (2010)
116. S. Richter, M. Heinrich, S. Döring, A. Tünnermann, S. Nolte, *J. Laser Appl.* **24**, 042008 (2012)
117. M. Beresna, M. Gecevičius, P.G. Kazansky, *Opt. Mater. Express* **1**, 783 (2011)
118. M. Beresna, M. Gecevičius, P.G. Kazansky, T. Taylor, A. Kavokin, *Appl. Phys. Lett.* **101**, 053120 (2012)
119. F. Messina, E. Vella, M. Cannas, R. Boscaino, *Phys. Rev. Lett.* **105**, 116401 (2010)
120. E.S. Efimenko, A.V. Kim, *Phys. Rev. E* **84**, 036408 (2011)